Thermal Analysis of a Vacuum Sealed Flywheel

Andrey Feliciano de Oliveira

School of Engineering

Thesis submitted for examination for the degree of Master of Science in Technology.
Espoo 27.04.2021

Supervisor

Prof. Martti Larmi

Advisor

Maksim Sokolov

Aalto University
School of Engineering

Aalto University
School of Engineering

Aalto University, P.O. BOX 11000, 00076 AALTO
www.aalto.fi
Abstract of the master's thesis

Author Andrey Feliciano de Oliveira

Title Thermal Analysis of a Vacuum Sealed Flywheel

Degree programme Advanced Energy Solutions

Major Sustainable Energy Conversion Processes **Code of major** ENG3069

Supervisor Prof. Martti Larmi

Advisor Maksim Sokolov

Date 27.04.2021 **Number of pages** 49 **Language** English

Abstract

The purpose of this thesis is to analyse the thermal control for a flywheel energy storage system, used to harness electric energy as mechanical rotational energy. The work is to be used as reference to possible improvements to be made in the next iteration of prototyping to meliorate the efficiency of the overall system.

The thermal system is designed and analyzed under vacuum conditions. The heat transfer is simulated in ANSYS Fluent and Thermal and compared to the real-world system. Additionally, the analysis compares two states of operation, under vacuum conditions and under atmospheric conditions.

All losses from the motor are converted into heat, and the hollow windings are used to pump the cooling fluid in the active coils. The heat generated at the motor assembly due to copper losses and hysteresis losses as the permanent magnet machine rotates around a ferrite core, is calculated and compared to the real world heat measured by the rising temperatures at the cooling fluids.

The most temperature sensitive components are the permanent magnets found at the top, center and bottom of the rotor which have a demagnetization temperature of approximately 150°C. Additionally, the rotor is a composite of carbon fiber and resin, which has a curing temperature of around 140°C. As the rotor operates under full levitation, the only means to dissipate heat from the rotor is via radiation to either the external housing, or the outer face of the stator. The results suggest that the overall system could experience high temperatures at longer operations, therefore improvements are required. Suggestions are proposed for future iterations of the machine to enhance the performance and efficiency of the overall system.

Keywords ANSYS Thermal, Flywheel Energy Storage, Internal cooling, Electrical machine losses

Preface

The thesis work was done during the flywheel prototype design and assembly from September 2019 to February 2021. The work accomplished at Teraloop is still under development and with many technical strives we achieved 7000 RPM as of February 2020. The thermal analysis performed with simulations are but an estimate to get the machine in working condition as no work in these specifications was ever performed. The team, both engineering and business side, have made massive milestones in light of a historic year 2020. This paper would not have been accomplished without the help of: Markus Merilä, our great Chief-engineer who led the discussion and implementation of Prototype-2, Juuso Pöllänen and Neha Chohan, our commissioning super-stars, Syed Kazmi, for his knowledge in electromagnetism and losses calculations, Maksim Sokolov for the guidance and the suggestions, Professor Martti Larmi for the suggestions and patience, and of course the remainder of the team who supported the project and still push the company forward during these uncharted times.

Otaniemi, 27.04.2021

Andrey L. Feliciano de Oliveira

Contents

List of Figures

List of Tables

Abbreviations and symbols

Abbreviations

AC	alternating current
AMB	active magnetic bearing
FEM	finite element analysis
FESS	flywheel energy storage system
GHG	green house gases
PM	permanent magnet
PMSM	permanent magnet synchronous machine
RPM	revolutions per minute
SMC	soft magnetic component
VFD	variable frequency drive

Symbols

α	Angular acceleration
η	Efficiency
ν	Poisson's ratio or kinematic viscosity
ω	Angular velocity
ρ	Density
σ	Stress
σ_B	Stefan-Boltzmann constant
σ_r	Radial stress
τ	Torque
θ	Angular position
ε	Emissivity
a	Acceleration
A_c	Cross-sectional area
A_s	Surface area
B	Magnetic flux density
B_{max}	Maximum flux density
c_p	Specific heat capacity
D_h	Hydraulic diameter
F	Net force
f	Frequency or Colebrook friction factor
g	Gravitational acceleration
H	Magnetizing force
h	Convection heat transfer coefficient
h_f	Frictional head loss
E_{kin}	Kinetic energy
E_{in}	Energy input
E_{motor}	Energy of motor
E_{losses}	Energy loss
E_{out}	Energy output
k	Thermal conductivity
K_h	Steinmetz constant
K_e	Eddy current constant
m	Mass
N_s	Synchronous speed
Nu	Nusselt's number
P	Power
P_{copper}	Copper loss
P_{eddy}	Eddy current loss
P_{hys}	Hysteresis loss
P_{loss}	Overall magnetic loss
$P_{cooling}$	Overall cooling power
p	Pressure
Q_{cond}	Conductive heat
Q_{conv}	Convective heat
Q_{gen}	Generated heat

r	Radius
r_i	Inner radius
r_o	Outer radius
Re	Reynold's number
Pr	Prandtl's number
T	Temperature
T_s	Inner wall temperature
T_m	Mean temperature
v	Velocity
V	Volume
x	Length
W	Work
dT	Differential unit of temperature
dx	Differential unit of length
$\dot{m}$	Mass flow rate
$\dot{V}$	Volumetric flow rate

1 Introduction

The world is struggling to maintain the global temperature rise to below 1.5 °C as agreed in the 2016 Paris Agreement. Currently, fossil fuels remain the primary source of energy at a staggering 81% of the world's energy supply [9]. Much effort has been made to decrease green-house gas emissions with continual increase in solar and wind installations. With 19 GW of installed Solar and wind energy sources in 2019, production is expected to more than triple in the coming 5 years [10]. This calls for a void in the energy market as flexible means of storage could help stop curtailment. This alone would further aid the expansion of solar and wind which leads to a larger demand for storage. According to some sources, storage could go as far as becoming the 4th pillar of the energy cycle along with generation, transmission and distribution.

With such an expansion and changing of the energy market, many storage options have stood out as having a bright future. Namely, Lithium-ion batteries, pumped storage, supercapacitors, power-to-gas, and flywheels.

One of the newer methods for storing energy is the Power-to-Gas conversion of electrical energy into hydrogen or methane gas with the use of polymer electrolyte membrane or reversible Solid Oxide Fuel Cells. This conversion is, however, drastically inefficient and would require space to store the hydrogen gas safely.

Pumped storage is a clever way of storing electrical energy in the form of potential gravitational energy. It works in the form of two large reservoir tanks of water at different heights. When energy is needed, the water flows from the top reservoir to the bottom and passes through a generator in the form of a water rotor propeller. When electricity is in lower demand, and hence cheaper, the water is then pumped back up from the bottom reservoir to the top reservoir. This storage method is very effective, however, it comes at the cost of placing the reservoir in large areas and it is not optimal for all locations. This means the energy density of the pumped hydro storage is significantly less than other methods.

Chemical batteries such as Lithium-ion batteries are a method of converting electrical energy into chemical energy by usage of potential chemical reactions. Lithium-ion batteries are currently the most common way of storing energy and much development has been done to improve the energy density and the lifespan of batteries. Major players such as Tesla and LG have announced production of large facilities where gigawatt sized production capability is to take place. Although the batteries are likely to dominate the energy storage industry, much effort still needs to take place to improve the longevity of the battery packs as they fall short of the high cycles required for many applications and the environmental impact of the raw material extraction of the batteries.

The flywheel is a kinetic energy storage device that utilizes a spinning rotor to store energy as rotational inertia of the rotor. The electric energy comes from the grid to the electric motor drive of the rotor, which is in turn, used to rotate the cylindrical mass. The flywheel energy storage system (FESS) can be thought of as a mechanical battery, as it speeds up, the flywheel charges up, and when the energy is required, the flywheel is slowed down and the mechanical energy is converted

to electrical energy and fed to the grid. Traditional flywheels consist of a rotor physically attached to a central shaft and supported by bearings on each end of the shaft. This configuration is great for scaling the energy capacity, however, requires a large amount of area for this adaptation. A hubless flywheel is the next concept that allows the flywheel to rotate at higher speeds by increasing the stress limitation of the rotor itself. Additionally, a fully levitated rotor, radially and axially stable, intakes less frictional losses. In comparison to about 5% losses of mechanical bearings, active magnetic bearings have 1% loss of total power [18].

The market in this case would require sustainable way to ramp up production of a storage system, and for Lithium-ion batteries that would mean a serious amount of mining something known as GHG emission intensive. A scalable alternative could be a kinetic energy storage device.

2 Motivation

The thermal aspect of rotary machinery in particular electric motors is vast in terms of analytical work. Loss analysis and efficiency maps are no news to any seasoned electric motor designer. These are some of the first things thought of when producing a permanent magnet synchronous machine. The topology, winding scheme, operational environment and size ultimately play a role in determining the type of machine and its performance. However, experimental data and real-world validation is a common wish in many peer reviewed articles regarding the topic. The loss identification is difficult in practice, so any findings are considered carefully. The purpose of this paper is to allow for better understanding of the loss parameters in a flywheel design to eventually make a product out of the prototype.

This brings us to Teraloop's audacious solution to reinvent the wheel. Carbon fiber is used in place of steel or concrete, allowing the rotor to undertake more radial and tangential loads at higher speeds, while decreasing the physical size of the rotor. This in turn effectively augments the energy density tenfold. For a small cabinet size flywheel, one can store 3-5kWh of energy at a power of 100kW. The 100kg rotor includes segments for each subsystem reflected on the central hub, the stator. The rotor is driven by a permanent magnet synchronous machine, where magnets embedded on the rotor lock into place with a rotating magnetic field created by an AC motor stator assembly. When discussing motors of above 90% efficiency, the last optimization of losses come from a variety of types, but ultimately one output, heat. In addition to that, active magnetic bearings (or AMB), which stabilize the rotor also require windings and therefore more losses as heat generation. The supersonic speeds require a vacuum seal for the rotor as air drag losses dominate above the speed of sound. The vacuum essentially traps the thermal energy which can overheat sensitive parts and irreparably damage the flywheel assembly. The focus of this paper is on the design and efforts made towards the active cooling system. The thermal analysis performed with ANSYS modelling is used to estimate the thermal losses taken on the rotor and in turn mitigating them on the stator side and surrounding housing. This project is ongoing at the time of writing this, therefore the findings are being used in an iterative method to the system.

The thermal analysis performed in this paper are an attempt to improve the performance of the motor-generator assembly and reduce the overall temperature of the system as some sub-assemblies are specially susceptible to damage at temperatures higher than 150°C. The laser sensors used to identify the position of the rotor, the rotor's resin's curing temperature, and the magnets used for the passive axial levitation, all lie around 150°C. These alone help determine the temperature limits required for the prototype to become a viable product and the success of commissioning the machine in a pilot event.

Figure 1: Teraloop Prototype-2

3 Background

3.1 Mechanical

The flywheel technology is ultimately a physical embodiment of energy. This is achieved by utilizing simple, yet fundamental mechanical laws explained further in the next sections.

3.1.1 Energy Transfer

A simple allegory to understand flywheel is to refer to it as a mechanical battery. Where the electrical energy supplied in terms of current and voltage are transferred to mechanical momentum and hence, mechanical energy. Mechanical kinetic energy is defined by the movement of a certain mass (m) at a certain speed (v):

$$E_{kin} = \frac{1}{2}mv^2 \tag{1}$$

As defined by Sir Isacc Newton, any body of mass remains at rest or at constant velocity unless acted upon by an external force. In turn, a specific amount of energy is required to produce the aforementioned force. By using Newton's 2nd law of motion, force is identified as:

$$F = ma \tag{2}$$

where F is the force required to accelerate a mass m at an acceleration of a. Furthermore, work, or the amount of energy displaced over a length x due to an applied force F can be defined as the following:

$$W = Fx \tag{3}$$

For a body rotating around a fixed axis, a tangential force will, in turn, have a torque associated defined by

$$\tau = Fr \tag{4}$$

where τ is the torque produced by a tangential force F at a radius r.

At this point it is wise to convert the linear terms such as x, v, a, and F into rotational components of $\theta, \omega, \alpha, \tau$. With this change and applying Torricelli's equation of motion to replace the angular displacement θ, equation 3.3 becomes

$$W = \tau d\theta = mr\frac{d(\omega)}{dt}\theta = mr\alpha\theta = mr\alpha\frac{\omega_1^2 - \omega_2^2}{2\alpha} \tag{5}$$

which simplifies to:

$$W = \frac{1}{2}mr\omega_1^2 - \frac{1}{2}mr\omega_2^2 \tag{6}$$

The right hand-side can then be replaced by the initial equation 1. When tying together the energy equation to the work done to the flywheel by the electric motor:

$$W = E_{kin1} - E_{kin2} \tag{7}$$

The overall energy balance then becomes the electric energy being inputted by the motor and the work done by the rotor equated.

$$E_{in} = E_{motor} - E_{Losses} \tag{8}$$

In reality the energy equation includes minor losses as the real systems always acquire some losses during energy transition which will be explained later in this chapter. Equation 6 details the relationship how the amount of energy one is able to store in a flywheel is dependent on the mass and the speed at which the body is rotating. In order to increase the capacity of a flywheel, one must either increase the mass of the flywheel or increase its rotational velocity. It was an obvious option to increase the speed of the rotor over increasing the mass, as the velocity component is squared and therefore has more of an effect on the overall capacity. The only concern is then what kind of material can withstand such high centrifugal forces without complete failure of the rotor due to internal stresses.

3.1.2 Material Stress

As the flywheel speeds up and spins, the material of the flywheel experiences stress due to the centrifugal force of the body itself.

$$\sigma = \frac{F}{A_c} \tag{9}$$

The stress stems from the fact that any mass rotating experiences a tangential force as its mass essentially is being pulled apart. This is ultimately the limiting factor in traditional flywheels which are manufactured as a full steel cylinder. The radial stress component in turn decreases the ultimate speed of the flywheel and consequently the amount of energy stored by the system. Hoop stress is the term identified with a cylindrical structure rotating at its center axis and it is defined as follows:

$$\sigma_r = \rho\omega^2 \frac{(3+\upsilon)}{8}(r_i^2 + r_o^2 - \frac{r_i^2 r_o^2}{r^2} - r^2) \tag{10}$$

As seen by the above equation, the stress is minimized when the ratio of inner diameter to outer diameter is closest to 1 [3]. A ring or a hollow cylinder effectively decreases the maximum stresses seen by the body and thus allows the structure to operate at higher speeds, which in turn increases the energy storage capability for a similar volume.

3.2 Electromagnetic

3.2.1 Power

In order to begin rotating the body, or flywheel, an external source of energy must be identified. Electric motors in our case are the best way to initialize the process. In addition to providing quick and efficient power to the rotation, the motor can also

be operated as a generator simply by reversing the process. Power is then defined as the amount of instantaneous energy needed to keep the rotating body spinning at a given fixed torque. The equation is as follows:

$$P = T\omega \tag{11}$$

For electric machinery, a torque-speed curve can be devised with an efficiency associated with each.

3.2.2 Magnetism and motor principles (PMSM)

The studied flywheel motor subsystem is a Permanent Magnet Synchronous Motor (or PMSM). The rotor side of the motor subsystem is composed of a constant magnetic field with alternating poles of a hard magnetic component, neodymium permanent magnets. The stator of the motor subassembly supplies the revolving magnetic field via a 3-phase AC source. The stator is wound as a concentrated wound motor and the supplied current drives the machine with 8 poles and 3 phases. The stator has 12 slots so there are 4 windings per phase.

On the rotor side, magnets are located at the same plane as motor stator in order to provide a constant magnetic field on the rotor side. The magnets are setup to have 8 alternating poles on the rotor. When operation begins, alternating current is fed in the stator windings creating a rotating magnetic field. The opposing poles in the rotor are attracted to the newly generated rotating magnetic fields of the stator, and once the torque generated by the attraction of poles overcomes the polar inertia of the rotor, the rotor begins to rotate with the same frequency as the revolving field. The field is rotated at synchronous speed. The synchronous speed is defined by the following equation:

$$N_s = \frac{120f}{P} \tag{12}$$

where N_s is the synchronous speed (in rev/min), f is the frequency of the supplied current, and P is the number of poles. [13] The rotational speed of the rotor is therefore dependant on the number of poles and the frequency of the motor drive. As the motor drive is an expensive component and was previously defined, the only way to increase the synchronous speed and consequently the operating rotational speed, is to minimize the number of poles. The downside of decreasing the number of poles was the need to account for the pole pitch, or the distance between each pole, where a stator core needs to interact in order to prevent stalling of the rotor. Luckily, the Prototype-2 design was intended to maximize energy density, so the diameter of the rotor was decreased from the previous prototype, and this played in favor for the pole pitch.

Another aspect to take into account is the inverse relation between torque and speed. As the speed of the machine increases, the available torque decreases. The system was designed with constant power mode in mind, meaning that the rotational speed of the system would not be limited by the available torque. Prototype-2 in essence is a power machine and its purpose is to store energy and output the

most power possible in the smallest space possible. Hence, the rotational speed was maximized, not the torque availability. A further look into the system's parameters is in Chapter 5.

3.2.3 Losses

With any real-world system, the overall efficiency determines not only how well the system behaves, but also informs the amount of losses expected which translate mostly into heat. For electric machines, specifically the PMSM, the motor losses come in two forms: iron losses and copper losses.

The iron losses mostly come in hysteresis and eddy current losses. Hysteresis losses come from the magnetic retentivity of the material. A soft magnetic material, such as electrical steel, can be magnetized and demagnetized. For this to happen a magnetizing force must be applied to realign the domains of the material into poles and create a magnetic flux. The current applied in the copper surrounding the iron core is a source for this magnetizing force. Additionally, in the idling phase when the motor is off, the PM in the rotor serve as revolving magnetic field. This is microscopic event reshapes the magnetic zones of a material to either South pole or North pole. When the magnetizing flux density decreases the soft magnetic material's flux density does not decrease at the same rate. In fact, a certain amount of flux remains in the core known as the retentive flux. When the AC current is completely reversed it applies a magnetic force of equal strength but in the opposite direction, forcefully demagnetizing the iron core. A hysteresis loop (figure 2) is therefore a 4 quadrant graph that shows the relationship between this magnetizing force (H) and the flux density (B) of a material. The area inside the loop is the amount of energy required to fully magnetize and de-magnetize a material one cycle. With electric motors, these cycle events can occur over 2400 times per second (or 2.4kHz).

These losses due to the retentivity of the material are defined by the following equation [15]:

$$P_{hys} = K_h f^a B_{max}^b \tag{13}$$

where f is the frequency of the magnetic reversal, B_{max} is the magnetic flux density, and K_h, a, b are Steinmetz constants that come from the particular material's B-H curve and are empirically derived.

In addition to the hysteresis losses, the electrical steel in the stator experiences eddy current losses due to Faraday's Law, or change in magnetic environment causing an indulced voltage in the conductor. This induced voltage, or EMF, causes corresponding currents to circulate, known as eddy currents. The eddy current losses are minimized by manufacturing the stator core from many thin sheets, or laminations, that break the flow of the eddy currents. Eddy current power loss is commonly calculated by using the following formula:

$$P_{eddy} = K_e B_{max}^2 f^2 t^2 V \tag{14}$$

where t is the material thickness (in m), V is the volume of the material in m^3, K_e is the eddy current constant

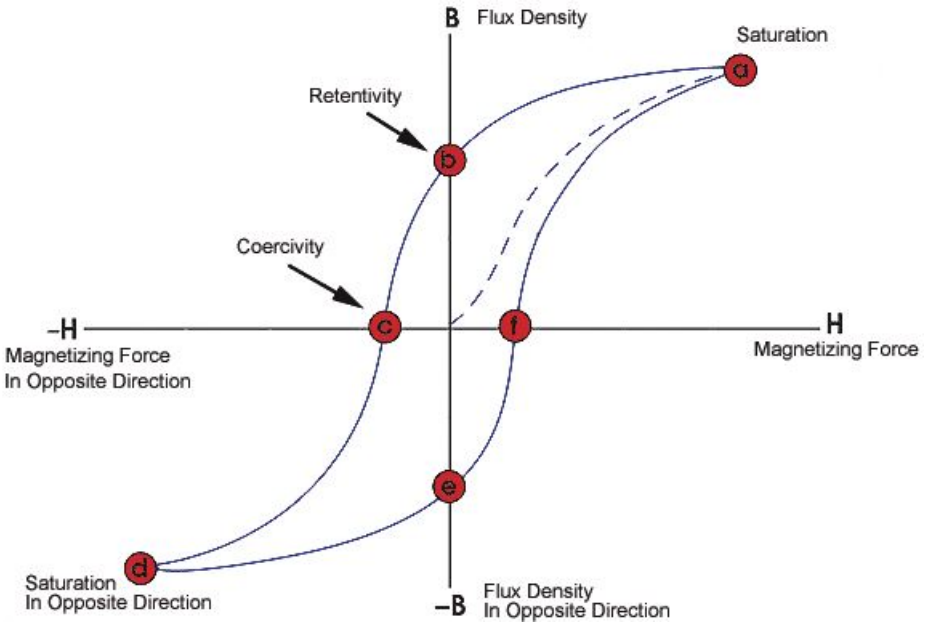

Figure 2: Hysteresis loop example

From the overall motor losses the iron losses are seen mostly at higher speeds of operation as the rotating magnetic field increases the hysteresis losses as the field switches faster. Additionally, it is common practice to take the loss data obtained from the electric steel core manufacturer in order to establish an expected loss coefficient due to all the possible rotational losses. For the material selected, M270-35A, the core losses at 2500 Hz (similar to the prototype's effective frequency) and a field of 0.5 T, the expected total iron losses are of 79.1 W/kg [6].

Copper losses are heating losses from the resistance of the winding material. As the electrical current passes the copper, the atoms are excited and move, causing heat. This loss is dictated by I^2R.

By applying the formulas above, an estimation of the major losses can be summarized in the following equation:

$$P_{loss} = P_{hys} + P_{eddy} + P_{copper} \tag{15}$$

The efficiency map of the rotor takes the speed and the torque into account allowing to visualize the efficiency of the system operating. Under our conditions it the expected efficiency during operation is of approximately 96%. For a 100kW motor with losses of 4% in heating, this results in 4kW of expected losses that need to be removed by the motor alone.

As heat is generated and dissipated across the system, it is imperative to understand the underlying mechanisms that allow this phenomenon to occur. In order to maintain the rotor below a specific temperature, the subsystems must allow the heat to be dissipated and ultimately released in an efficient manner.

3.3 Thermal

3.3.1 Conduction

Conduction is the process of heat transfer between two bodies in contact. This heat transfer also occurs within a single body and it is the main form of heat transfer within solid bodies. At a molecular level, it is the energy transfer due to vibrations in the solid atomic structure. The heat transfer rate defined as Q can be expressed by Fourier's Law in the equation:

$$Q_{cond} = kA_c \frac{dT}{dx} \tag{16}$$

Where k is the thermal conductivity (in $\frac{W}{Km^2}$), a material property, A is the cross-sectional area of the body and $\frac{dT}{dx}$ is the the temperature difference over a defined distance. The only constant in this equation is k, which can only be controlled by material selection. The heat transfer rate is therefore directly proportional to the cross-sectional area and the temperature difference, but inversely proportional to the dx, length. This means that for the highest possible heat transfer between two bodies, it is best to maximize the area of contact A, and the temperature difference between the two dT, while minimizing the perpendicular length (or height) of the bodies dx[2].

For our system, conduction occurs in any places which have direct contact with one another as all subsystems are stacked on top of each other. This means the heat generated due to motor and AMB losses is then diffused to the stator as the windings heat up and are in direct contact with the actuators. From the actuators, the heat transfers to the inner stator stack, where minimal heat transfer then occurs to the housing from the bottom and top plate.

3.3.2 Convection

Convection is the heat transfer between fluids and a solid body, or two fluids. This type of heat transfer is due to the random motion of fluid particles over a body, or diffusion, and energy transfer by the bulk fluid motion, or advection. There are two main cases of convection, 'free' and 'forced' convection. Free, or natural, convection refers to the fluid movement due to temperature differences in the fluid. As density is temperature dependent, the hotter parts of fluids naturally rise, and the cooler fluids sink, this then leads to bulk movement of the fluid. In forced convection, the movement of the fluid is due to an external force, such as a pump [4]. Forced convection is used to enhance the heat transfer of a system and therefore is the convection type of interest for this paper.

For the internal flow conditions observed by the motor hollow windings, Newton's law of cooling can be applied to determine the heat transfer rate between the coolant and the copper:

$$Q_{conv} = hA_s(T_s - T_m) \tag{17}$$

where T_s is the surface temperature of the inner wall of the winding, T_m is the mean temperature of the cooling fluid, A is the heat transfer surface area and h is the local convection heat transfer coefficient. This convection coefficient variable is imperative to determine the efficacy of the heat transfer occurring and can be found by using Nusselt's number, a dimensionless number that is the ratio between the convective heat transfer and the conductive heat transfer in the boundary layer between the copper surface and the fluid.

To find the appropriate Nusselt's number, the following must be established:

- The flow is fully developed as the entry length is far from where the heat convection is occurring.
- There is a constant heat flux ($Q_{gen} = constant$)
- Reynold's number determines the flow to be turbulent or laminar. In this case the flow is turbulent ($Re = 5717$)
- Prandtl number for water is 3.56 at 50°C

The following equation can then be used:

$$Nu_D = \frac{(f/8)(Re_D - 1000)Pr}{1 + 12.7(f/8)^{1/2}(Pr^{2/3} - 1)} \tag{18}$$

where f is the Colebrook friction factor, used to estimate the pipe frictional losses, Re is the Reynold's number, and Pr is the Prandtl number, a dimensionless number used to calculate the ratio between viscosity and thermal diffusivity. Using this method gives a Nusselt number of 20.8 for the pipe flow. The Nusselt equation is also a ratio of the convective and conductive heat trasnfer and therefore can be written as:

$$Nu = \frac{hD_h}{k} \tag{19}$$

where D_h is the hydralic diameter of the pipe. When solving for the coefficient of convective heat transfer, the results are of a value of around 5000 $\frac{W}{m^2K}$. This value is later used in the simulation as an input for the convective heat transfer module. In an additional note, in forced convection the h value tends to lie between 50-10000 $\frac{W}{m^2K}$, so the above number is in line with typical values.

Going back to equation 17, the overall heat transfer dissipated by the forced cooling is calculated to be $Q_{conv} = 5.3$ kW. It is imperative for Q_{conv} to remain higher than the Q_{gen} created by the motor losses. For the cooling system to work effectively as it is designed, $Q_{cond} \geq Q_{gen}$. Q_{conv} becomes important when sizing the pump in the later section as this will dictate the flow velocity and therefore the size of the pump.

For our processes, our Q_s is of around 5.3kW of effective heat removal per coil by utilizing water. This means that for a system outputting 4.8 kW of heat as motor losses, our parameters for cooling are well within effective use and should be able to maintain a temperature below critical operation. This will be further validated by experimental results of motor temperature during operation.

3.3.3 Thermal Radiation

Thermal radiation is the heat transfer between two bodies due to electromagnetic waves emitted by one body and absorbed by another. This method of heat exchange is independent of any other medium such as gas or solid and therefore, can occur in a vacuum chamber. Anything that has a temperature above 0 K, or absolute zero, will emit thermal radiation. The output heat due to thermal radiation is determined by the following equation:

$$Q_{rad} = \varepsilon \sigma A_s T^4 \tag{20}$$

where ε is the emissivity of the body in question, or the quantitative percentage of thermal radiation leaving the body, σ is the Stefan-Boltzmann constant, A is the surface area of the body, and T is the temperature of the body.

The main objective for this calculation is to estimate the heat absorption of the heating rotor under vacuum, as the only mean of dissipating heat is via radiation between its surrounding surfaces. Due to the nature of operation, we know that the rotor will likely see some increase in temperature due to the radiating faces of the the motor face. The inner surface of the rotor and the motor teeth and windings face each other close to parallel with a very small gap. The surface of the rotor are also engulfing the faces of both the motor's and AMB's. This leads the rotor to absorb much of the generated heat.

The radiation between the rotor and the housing provides an idea of how much heat can be dissipated from the rotor and it is given under the following equation:

$$Q_{out} = \frac{\sigma(T_1^4 - T_2^4)}{(\frac{1-\varepsilon}{\varepsilon_1 A_1} + \frac{1}{A_1} + \frac{1-\varepsilon_2}{\varepsilon_2 A_2})} \tag{21}$$

Equation 21 is a case specific equation used to determine the heat transfer between an enclosed body and the surrounding face. In the equation, A refers to the surface area between the outer rotor face and the inner housing, ε is the emissivity of the carbon fiber and the emissivity of the stainless steel, T_1 and T_2 are the rotor temperature and housing temperature [4].

The same equation can be used to determine the amount of heat absorbed by the inner face of the rotor and the faces of the motor stator. This is used as a last check to verify that the amount of heat absorbed by the rotor is less than the amount of heat the rotor radiates to the housing.

3.4 System requirements for Flywheel Application

A sole carbon fiber wound cylinder won't spin by itself. The electric motor generator requires some permanent magnetic field in order to lock its rotating magnetic field. Therefore permanent Neodymium magnets are embedded into the inner face of the flywheel rotor. Additionally, other components are required inside the rotor in order to levitate, sense, and actively control the radial movement of the rotor. These segmented components have decreased the effective maximum stress the rotor can

take as the magnets have a much lower yield strength than the high strength carbon fiber used for most of the rotor.

By utilizing carbon fiber as the primary material in the manufacture of the flywheel, the radial stress is limited by the resin used in the composite. This is a consideration when embedding components for the sub-assemblies such as the permanent magnets for the motor/generator and the other segments for the AMB and backup bearing assemblies. The extra components add to the stress experienced by the rotor structure as they experience centrifugal forces as the rotor spins.

3.4.1 Rotor Design

To store the desired energy capacity at the given speeds of rotation, the material of the rotor was chosen as a carbon fiber wound cylinder and made into a composite with an appropriate resin. The carbon fiber itself can endure the radial and tangential stresses imposed during the operation while minimizing the expansion of the rotor diameter. The material specification is another discussion topic out of scope of this paper, however, the material thermal property needs to be considered as this will determine the upper limit of the temperatures. The most sensitive aspects of the rotor are composed of:

- Resin used in the composite rotor, with heat distortion temperature of 138 °C
- Neodymium magnets with demagnetization temperatures of 150 °C

These are taken into consideration of vacuum conditions and the radiation calculation performed in the radiation section above. Additionally, these will be the targets of the cooling system on the rotor side.

3.4.2 Stator Core

As the permanent magnets are located on the rotor, the stator requires a revolving magnetic field source. This is accomplished an electrical steel sheet cores surrounded by copper windings. Alternating current passes through the copper windings, creating a magnetic field. By using AC current this magnetic field oscillates between North and South with the same but opposite amplitude as its neighboring poles. This rotation once locked to the stationary poles of the rotor, transfers the electric energy into the kinetic energy of the rotor. The laminated steel used in the stator serves not only as a good method for transferring energy, but as a way to prevent eddy current losses during the transition [7].

For the 8 Pole, 12 slot configuration, the arrangement of the windings can be seen in Figure 3. For each phase (A, B or C) there are a total of 2 coils in series, which are in parallel to 2 other coils in series. Each of the phases is supplied by a variable frequency drive (or VFD), which converts the DC line supply into AC for the motor, or vice-versa when the flywheel is discharged.

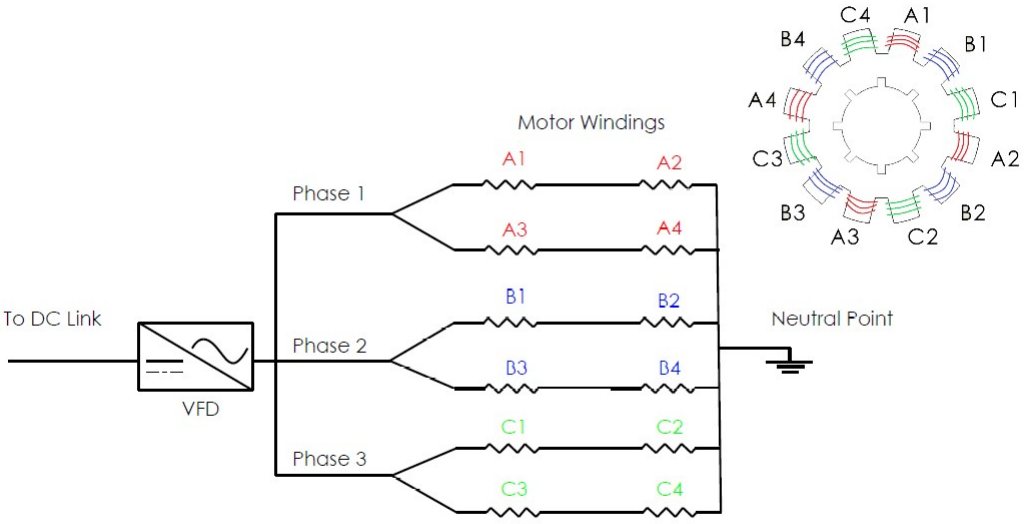

Figure 3: Winding and wiring for 12 slot/8 pole motor configuration

3.4.3 Stator Design

The size of the machine is depedent heavily on the size of the motor. As the rotor expands outwards with a void in the middle, it makes sense to design a radial flux motor to make use of all the space and create an energy dense machine. The motor sits in the middle of the symmetric rotor and thus has a size limit according to the rotor inner diameter. For Prototype-2 the rotor inner diameter was selected based on the overall energy and power requirements. The usable power was established as 100 kW and the energy storage was determined to be between 3-5 kWh depending on the rotational speeds of 18000 to 30000 rpm which would approach the absolute material stress limit of the rotor material. From there, the size of the motor was decided to fit inside the rotor inner diameter of 400mm. The height of the motor was then adjusted to match the required 100kW output. Additionally, the VFD supply frequency was limited to 600 Hz which helped determine the number of poles for the motor. The torque required for the 100 kW motor at a maximum speed of 18000RPM can be calculated as:

$$T = P\omega = 53Nm \tag{22}$$

This drove the efficiency limits for the machine and is further explained in Chapter 5.

The efficiency of the system is dependent drastically on the losses of the motor/generator transfer of energy. Any losses, thermal, vibration, will limit the machine performance. Therefore the subsystem requires great optimization and selection of materials. For main body of the core, electrical sheets are bonded together to

decrease the eddy current losses induced in the the core. For the coils, a hollow coil is used in order to allow the passage of a coolant fluid.

The PMSM is chosen due to its high efficiency for the high number of cycles in the particular application. A downside from the current design, however, is the continuous magnetic drag loss from the motor core. This decreases the idling time and effectively negates the storage aspect of the energy storage machine.

3.4.4 Pump sizing

The internal cooling is an essential part of the system for temperature control. In the internal lines of the electrical conductor runs a coolant fluid that is connected to a pump and illustrated in Figure 4. Each phase from the motor receives a cooling line that is powered by a pump. The sizing of the pump is the necessary step to determine the best economic and effective cooling options.

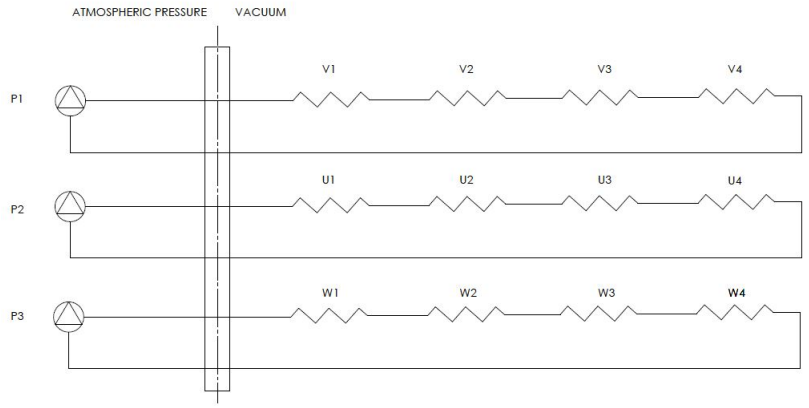

Figure 4: The three pump lines per phase

By using the energy-mass balance equation the energy needed to be dissipated must equal the energy it takes to change the temperature of a certain mass flow of water. In order to determine the size of the pump required, we must find the mass flow required to withdraw this heat.

The energy balance is as follows:

$$E_{in} = E_{out} \tag{23}$$

$$\dot{Q}_{gen} = \dot{Q}_{out} \tag{24}$$

The $\dot{Q}_{gen}$ term is directly calculated from the copper and iron core losses of the motor magnetic characteristics. The $\dot{Q}_{out}$ term is the derived from the convection of the mass flow of water through the conductor pipe.

$$\dot{Q}_{gen} = \dot{m}(c_p T_m + \rho\nu) - [\dot{m}(c_p T_m + \rho\nu) + \dot{m}\frac{d}{dx}(c_p T_m + \rho\nu)dx] \tag{25}$$

Which simplifies when assuming the coolant is incompressible and the derivative terms are and cancelling like terms:

$$\dot{Q}_{gen} = \dot{V}\rho c_{H_2O}\Delta T \tag{26}$$

The required head for the pump is a function of the required heat flux dissipation $\dot{Q} = 1.8kW$ per line, the temperature difference between entry and exit flow $\Delta T = 70K$, and the properties of the fluid being used, in this case water ($c_{pH_2O} = 4.2\frac{kJ}{kgK}, \rho = 1\frac{kg}{m^3}$).

From here the volumetric flow rate required can be determined from the energy balance equation. Assuming that all heat generated would be accounted for in the cooling, the velocity becomes:

$$\dot{V} = \frac{\dot{Q}_{gen}}{\Delta T * c_{pH2O} * \rho_{H2O}} \tag{27}$$

The volumetric flow rate of the coolant directly relates to the pump performance by relating the head energy required to overcome the frictional losses and also calculating the required pressure. Head loss and pressure are the basis for sizing the correct pump for a given application. Head is the height the pump can push the fluid and the pressure helps identify how much power the system will need per phase.

$$h_f = \frac{K_{sum}v^2}{2 * g} \tag{28}$$

The pressure for this amount of head energy follows as:

$$p = h_f\rho_{H_2O}g \tag{29}$$

which leads to the required power to overcome these frictional losses per phase:

$$P_f = p\dot{V} \tag{30}$$

where $\dot{V}$ is the volumetric flow rate and P is the pressure calculated in eqt. 30. the efficiency of the motor cooling loop can also be calculated by using:

$$\eta = P_{cooling}/P_{motor} \tag{31}$$

3.5 System requirements summary table

The table below (1) is a summary of the parameters set for our flywheel prototype. These are calculated values to later be compared with the actual system results.

For the real system, the measurements taken from the cooling water and the pump reservoirs are used to gauge how much energy was used to heat the reservoir and hence compared to the accuracy of the calculations.

Parameter	Value and unit
Motor output power	100kW
Motor efficiency	97%
Operational speed range	6000 - 18000 rpm
Torque	53 Nm
Temperature Limit	90° C
Heat Dissipation required per phase	2 kW
Volumetric Flow rate	0.41 $\frac{L}{min}$
Frictional head loss	18 m
Pump power per phase	1.2 W

Table 1: Prototype-2 calculation results

3.6 Literary review

The following is a summary of a selection of the papers that study the PMSM losses calculation. The topic is still widely researched and requires some more experimental data to verify all calculations.

In Sharkh (2019)[17] and Cho (2008)[5], a detailed description of the diffusion equation is used to build a foundation for analytical calculations of rotor losses. Further effort is made to analytically calculate the rotor losses using Poynting Vector. Additionally, 3D and 2D Finite Element Method (or FEM) is used to check the calculated results. Different case studies are performed in both to review the effects on rotor losses. Suggestions for minimizing rotor losses are discussed for example decreasing the slot gap and increasing the air gap. Careful design of the winding configuration appears as the cheapest and most effective solution.

In Mahmoudi (2015)[12] efficiency maps for electrical machines are derived using finite-element methods for defining the relationship between motor losses, torque, flux-linkage, current, and speed. The findings suggest that major loss components can be described using torque and angular velocity in a summation algorithm that accounts for different states of the machine. The results are then validated by comparing to three different machines and their efficiency maps.

In Huang (2019)[8] an innovative cooling system for an electric vehicle is examined and modelled. The hybrid cooling system incorporates a thermal jacket, fins and a fan to remove heat in an efficient manner via forced and free convection. Active control of the thermal system is performed in order to increase the efficiency of the heat dissipation and minimize power consumption. A simulation of an actual electric vehicle motor is incorporated and suggests that temperature can effectively be controlled by the proposed method and that the hybrid solution is more energy effective than conventional liquid cooling systems.

In Schaede (2014) [16] losses of a vacuum sealed, outer rotor flywheel energy storage system are analytically calculated and a lossmap is derived. The lossmap is composed of electric drive losses, active magnetic bearing losses. A method for calculating the AMB rotational drag losses is introduced which combines multiple traditional ways and includes penetration depth of the magnetic fields. Additionally,

an experimental measurement of the losses is performed in order to validate the findings of the lossmap. This paper is a great example of how to conduct the proper measurements in order to validate its calculated results and lossmaps.

In Nitsche (2017) [14] hollow winding conductors are introduced and direct cooling of the conductor is analyzed and compared to traditional motor configurations with a cooling jacket. The current density is estimated to be increased to upwards of 50 $\frac{A}{mm^2}$. With a more effective method for heat removal, the motors studied where able to double their torque density, effectively decreasing the size of the motor and simplifying the configuration of the machine.

4 Simulations

The thermal simulation was done in ANSYS Thermal and Fluent. For each of the simulations, an overall loss of 3 kW was assumed to go directly to the copper coils in the motor as heat flux. This means that each of the coils saw 250 W of constant heating. This value of 3 kW is taken as copper losses at the beginning of the run, and the currents seen during this process are higher than usual as the rotor requires a specific impulse of energy at the start to overcome cogging torque and initialize rotation of the rotor. This setup was taken to transient conditions and the motor and AMB (both heating components) were taken into account for the thermal simulation. Forced cooling in the motor coils was also simulated as forced convection with a coefficient of $[h]$. This simulation was initially performed to narrow down the temperature ranges seen in the machine. Once we gathered more information on the system and verified the losses of the machine, the simulation was improved. The preliminary simulation showed the temperatures of about 90° C at the motor. The most significant losses, and therefore, heat, is found in the motor teeth as iron losses and in the copper windings resistance losses. They are estimated to be 1 kW and 3.17 kW respectively. The heating caused by these losses raises the overall temperature of the system and require cooling in order to dissipate the heat. The heat removal is accomplished by using hollow windings on the motor and running a liquid coolant through it. As calculated in the previous chapter, the coefficient of cooling was determined to be 5000 $\frac{W}{m^2K}$ at its maximum.

4.1 Simulation Parameters

The parameters for the simulation setup were as follows:

- Internal heat generation at the motor coils due to copper losses
- Internal heat generation at motor teeth due to iron losses
- Heat conduction between coils and motor teeth and where applicable
- Convection at the motor coils due to active cooling (heat transfer coefficient conservatively estimated)
- Surface to surface radiation between the motor's teeth face and the inside face of the rotor
- Surface to surface radiation between the motor's coils and the rotor inner face

The 3D model for the simulation included materials similar to the actual machine and are presented below in table 2

4.2 Case Studies

In order to breakdown the heat generation into sectors, multiple different case studies were performed. The cases increased in complexity as additional elements to the

Component	Material
Rotor Composite	Intermediate Modulus Filament Wound Carbon Fiber
Rotor Motor Segments	Neodeneum Magnets N42 grade
Rotor AMB Segments	Soft Magnetic Composite
Motor Stator Core	M270-35A Laminated Electrical Steel
AMB Stator Actuators	M270-35A Laminated Electrical Steel

Table 2: Materials used in the ANSYS simulation

study were included. This way, each sub-assembly contribution is identified in terms of heat generation and heat dissipation.

4.3 Active Magnetic Bearing Heat Generation

In order to fully simulate the thermal effects of the machine, some subassemblies are needed to be included. In particular the Active Magnetic Bearing system needs to be included as it acts as another constant source of heat when the machine is running. The Active Magnetic Bearing system includes two coils, a bias and a control coil. The bias coil always has a constant amount of current flowing through it, while the control coil is mostly used to fine tune the position of the rotor and thus may not always be in use. The bias coil generates approximately 20 W of losses per coil which translates directly as heat. The AMB subsystem was first analyzed separately in order to establish individual temperature values that could later be validated with the experimental measurements. The component is then modeled as a heat source at the windings and contains a radiation diffusion from the surfaces that face the rotor. Below are the main simulation parameters for the case and their associated value in table 3

Parameter	Value
Heat generated per coil	$6.94 * 10^{-5} \frac{W}{mm^3}$
Rotor to AMB surface radiation emissivity	0.7
Initial temperature	22°C

Table 3: Isolated AMB simulation parameters

The heat generated per coil is a calculated value from the copper losses of the bias coil which always has 7.5 A of current running across it. One note is that the iron losses in the AMB cores are not included in this simulation.

The simulation was performed for a span of approximately 8 hours. This length in time was established as a duration long enough to reach steady state temperatures in the coils and rotor surface. The final temperatures observed inside the rotor and the AMBs are graphically represented in 5.

4.3.1 Motor modeling

The next step is to include the motor stator and windings to the model and include the copper and iron losses and the active cooling of the windings. By breaking the

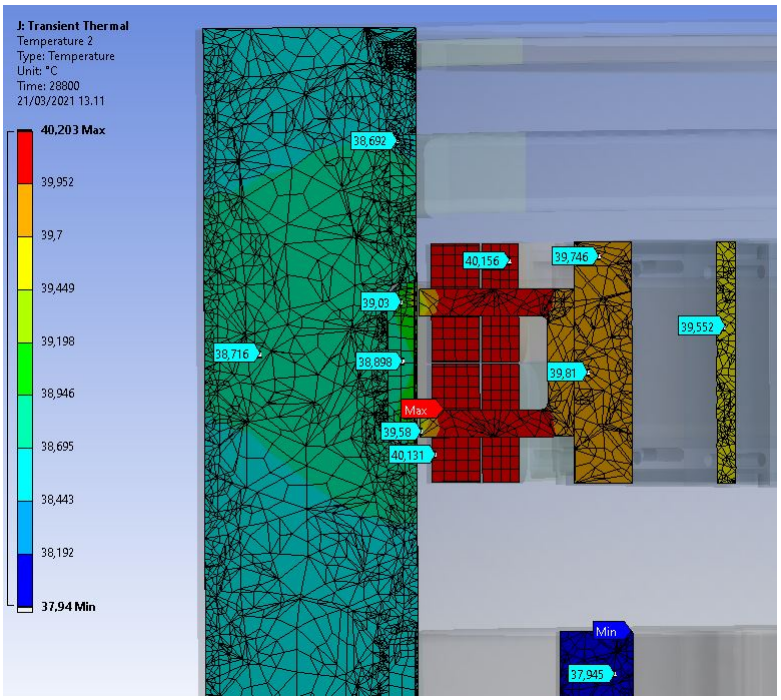

Figure 5: ANSYS results for thermal simulation

models up, it simplifies the model, allowing for a quicker check of values and different configurations. The motor subassembly experiences two types of losses as explained in the previous chapters, in addition to the heat removal process of the cooling lines. The copper losses are easily calculated to be 3,17 kW at its peak when currents are at their highest during ramp up. The iron losses are calculated by obtaining data from the manufacturer on the core losses of the M270-35A material. This is the most accurate and easiest way to estimate these losses as the manufacturer has taken the time to experimentally provide the values. For our 50 kg rotor, the core losses are then compiled to be 1,7 kW at its peak when the machine is rotating at 18000 rpm. Something to take note is the fact that the copper losses and the iron losses are not present at the same time. The iron losses are speed dependent and therefore are at their highest when the rotor is at full speed. The most realistic simulation setup was found to be:

Parameter	Value
Heat generated per coil	$6.94 * 10^{-5} \frac{W}{mm^3}$
Heat generated in iron core	$5.97 * 10^{-4} \frac{W}{mm^3}$
Convective heat coefficient	$3000 \frac{W}{m^2 K}$
Rotor to motor surface radiation emissivity	0.7
Initial temperature	22°C

Table 4: Isolated motor simulation parameters

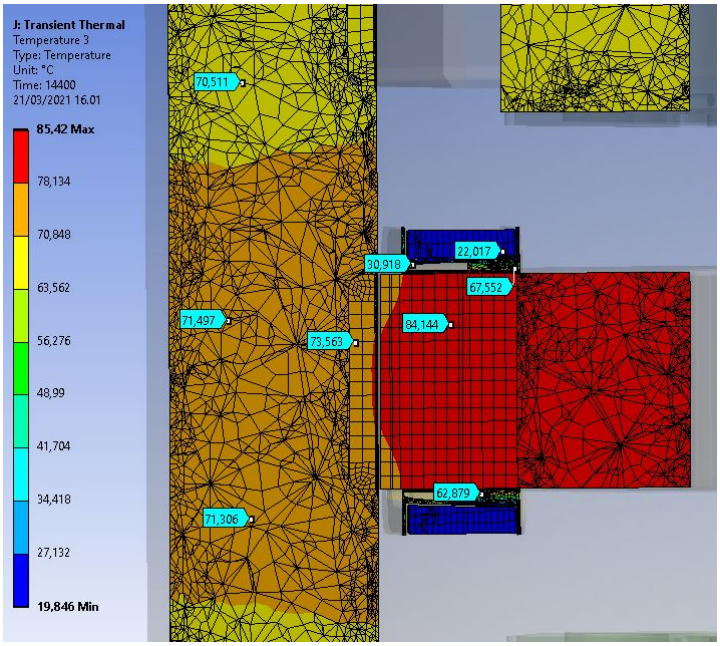

Figure 6: ANSYS results for motor only simulation, 4 hour

4.3.2 Motor Windings

As a final check of the motor sub-system, a more precise model of the motor windings and the inner fluid flow was checked with FEM. The 3-D model was improved by making every round of the winding distinguishable. Figure 7 shows the graphical enhancements. With a more accurate model, the fluid flow inside each round can be modeled with the help of Computational Fluid Dynamics (or CFD). ANSYS FLUENT, an industry-wide known, computational software was used for the simulation of the pipe flow. The conditions of the simulation are as follow:

- Inlet fluid velocity of 0.05 m/s;
- Heat generation of solid zone (copper zone) $2.6 * 10^{-1} \frac{W}{mm^3}$

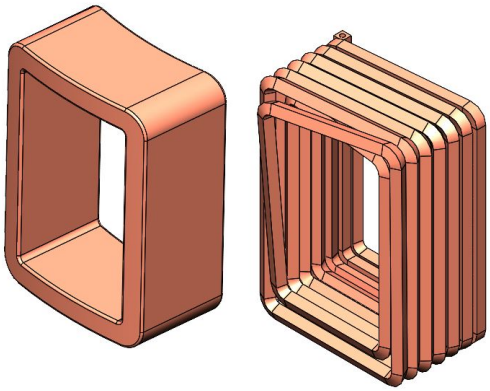

Figure 7: Improved motor winding models

- Steady state simulation performed
- The flow inside the pipes is fully developed and the $\kappa-\omega$ turbulence specification model is used to solve the continuity fluid flow equations.

The steady state simulation performed revealed the temperature range of operation and it can be seen in figure 8. The temperature range seen is based on the constant temperature of the coolant at the inlet of 21°C. With these results the temperature rise is lowest at the inlet and highest at the outlet around 120°C. These clearly show that the water cooling over a long duration is not enough, as the temperatures inside the winding should remain below the boiling point of water (< 100°C). The temperatures can also be decreased by increasing the flow of the coolant and increasing the size of the pump.

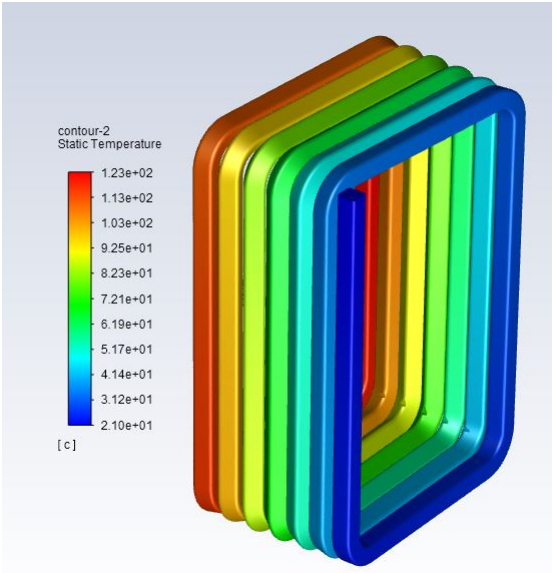

Figure 8: Steady state results for motor windings with internal cooling

4.3.3 Full System Modeling

The last remaining step was to introduce both motor and AMB subsystems in order to determine the overall system temperature. The simulation was performed with mostly iron losses and some copper losses as the operation would likely take place during a ramp up and remain at higher operational speeds between 6000 rpm and 18000 rpm.

The overall system modelling was the main goal of this study in order to give an estimate for the component heating during the vacuum runs. Table 5 is the setup used in the ANSYS transient thermal simulation.

Parameter	Value
Heat generated per AMB coil	$6.94 * 10^{-5} \frac{W}{mm^2}$
Heat generated per Motor coil	$1.87 * 10^{-5} \frac{W}{mm^3}$
Heat generated in iron core	$5.97 * 10^{-4} \frac{W}{mm^3}$
Convective heat coefficient	$3000 \frac{W}{m^2 K}$
Radiation emissivity between surfaces	0.7
Initial temperature	22°C

Table 5: Overall system simulation parameters

The convective coefficient of heating is slightly lower than 5000 $\frac{W}{m^2 K}$ as the cooling system's power supply is split by three pumps, effectively lowering the output pressure.

Figure 9 and 10 show the transient temperature results obtained from a thermal FEM simulation with an 8 hour time span.

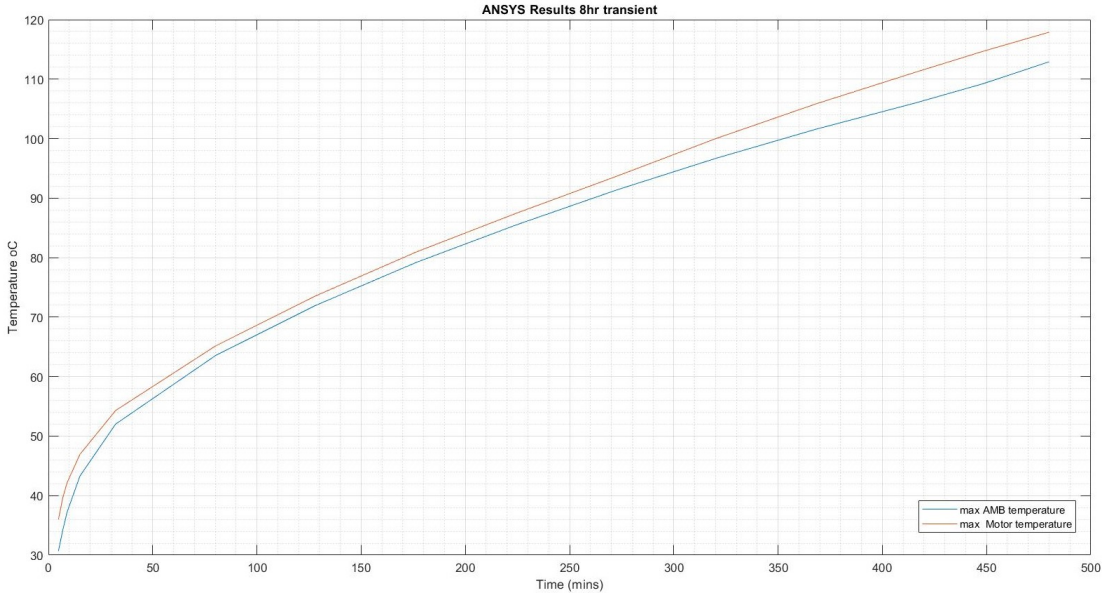

Figure 9: Temperature curves for overall thermal simulation

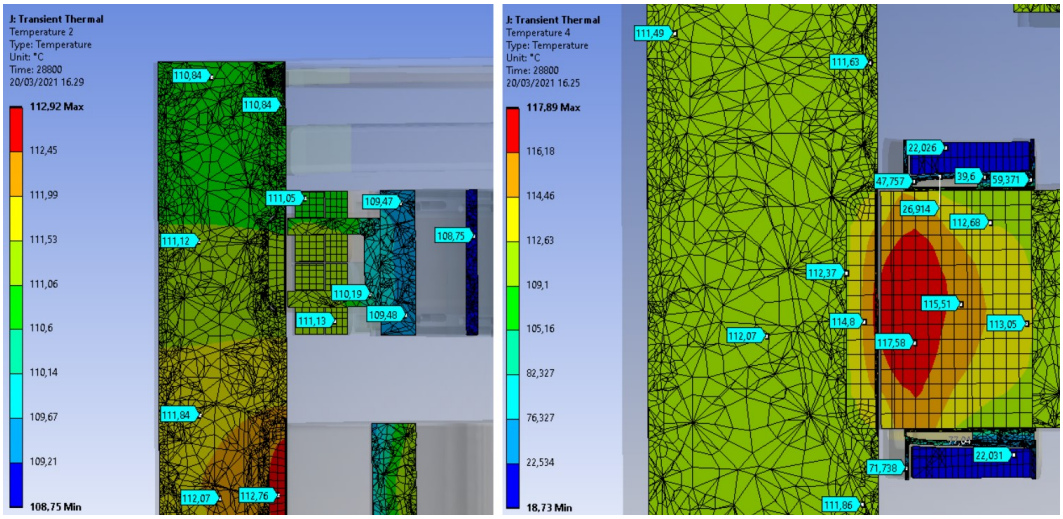

Figure 10: Slice views of AMB (left)and Motor (right)

As seen on the graphic, the rotor's temperatures are clearly affected and effectively raised due to the thermal radiation from the motor teeth. The highest temperatures are observed inside the teeth of the motor and on the surface of the rotor closest to the motor teeth. The values shown are an estimation and require further validation with empirical and experimental values observed when the machine is operated in vacuum conditions.

The final results give a maximum temperature of 114°C for the rotor, 117°C for the motor stator, and 111°C for the AMB coils after 8 hours. If the real experimental results are close to this analytical results, the cooling system would be considered a success for this operating time frame. The temperatures remain well below any

dangerous demagnetization temperatures of 150°C or resin curing temperatures of around 140°C. These results will be later compared with the data collected during ramp ups of the actual prototype machine.

The thermal simulations give a good idea of how the heat is radiating to the rotor, and although the values are likely lower than actual, it serves as a good study on the areas that require the most attention when optimizing the cooling system. Ideally, further iterations of the simulation are performed and validated experimentally in order to obtain a reasonable model than could be used in future projects as a basis for thermal analysis and help optimize the system without having to spend money on over-sizing the cooling system for larger machines in the Megawatt scale.

5 Experimental Results

5.1 Motor Assembly

For Prototype 2, the permanent magnet synchronous motor was selected as it offers high efficiency, can be used with standard VFDs and it has been used in the previous prototype, therefore, had a lower technological risk. One of the disavantages of the PMSM in comparison to, for example, a switch reluctance motor, are the idling losses, since for the PMSM the rotor magnetic field losses cannot be switched off.

The motor was designed to have 100 kW output power at an operational speed of 18000 rpm. The actual output power is approximately 120 kW in order to achieve 100 kW at any given operational speed. The winding is a layered concentrated winding with two parallel lines per phase (see figure 11).

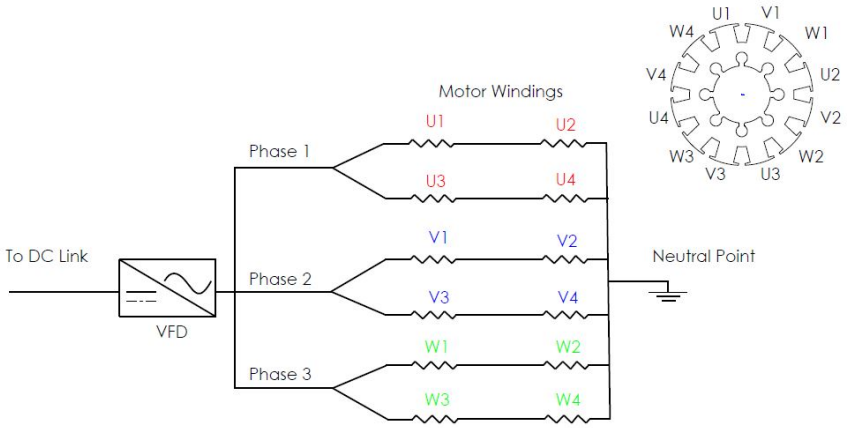

Figure 11: P2 motor concentrated wiring

This choice was identified by checking the optimal winding factor for a 8 pole 12 slot motor configuration [19]. The physical size of the assembly had to be considered as well when defining the winding scheme in order to decrease the overall height of the motor assembly and knowing the hollow conductors would be used and therefore required more space than the traditional conductors. Additionally, it is assumed that the current densities are around 15 A/mm^2 which are achievable but will require the cooling system in order to maintain the temperatures at a desirable level. A summary of the motor characteristics and estimated losses are summarized in table 6. The copper losses and iron losses are speed dependent and do not appear at their maximum at the same time. In addition, the iron losses are higher at the higher speeds as the hysteresis losses are proportional to the rotational speed of the rotor.

Motor Parameter	Value
Machine type	PMSM
Rated speed	18000 rpm
Output power	120 kW
Mean torque	65 Nm
Copper losses	3.17 kW
Iron losses	1.72 kW
Efficiency at nominal speed	96%

Table 6: Prototype-2 motor parameters

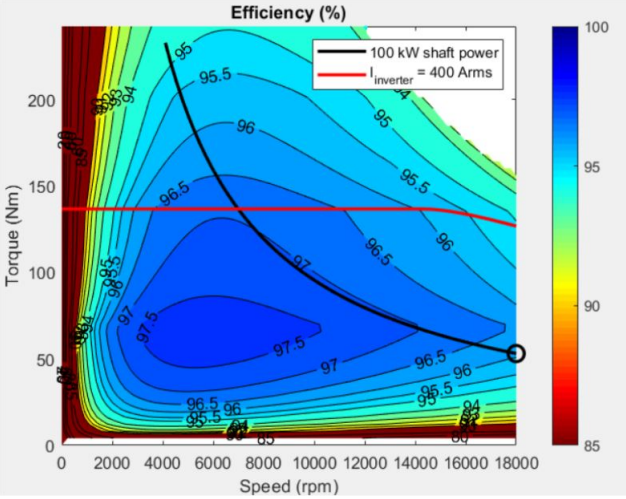

Figure 12: Efficiency map with inverter rating of 400 A and top speed of 18000rpm

The motor sub-assembly performance analysis was done via finite element analysis with the intention of estimating the efficiency of the motor throughout the operational range. The map was acquired by visualizing a constant 100 kW load output for the motor and overlayed with the inverter current limit of 400 A, and the efficiency at each operational point based on calculated losses. As observed in figure 12, the cutoff speed of the motor is approximately 7000 rpm for an constant output power of 100 kW, below which, the motor will decrease in effective output power due to the inverter current limit. Additionally, it can be seen that the operational zone of 7000 rpm to 18000 rpm will offer a 96% efficiency of the machine.

The actual winding of the motor was done by hand utilizing Luvata 8206 [11] hollow windings. The process was finalized (figure 13) and the motor coils passed a continuity test and a resistance check. The assembly proved to be arduous and towards the end of the windings much force was required to bend the last couple turns.

5.1.1 Motor Temperature measurements

In the first few runs tested, Prototype 2 was operated with atmospheric conditions. This was chosen as the tests were performed at low speeds and in order to see

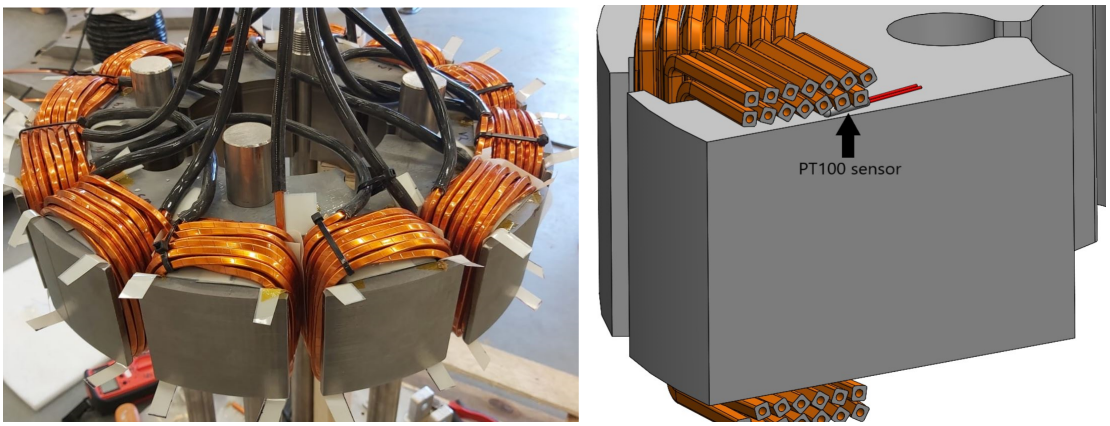

Figure 13: Prototype-2 motor assembly (left) and PT100 locations (right)

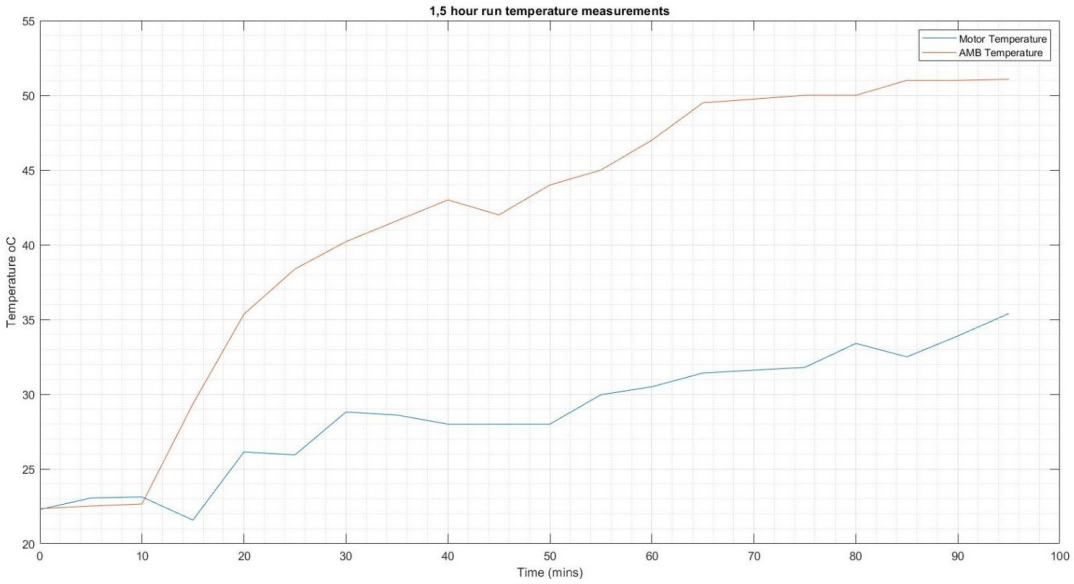

Figure 14: Prototype-2 recorded temperature

significant impact due to air drag, the rotor would need to be rotating at about 12000 rpm (to have a supersonic speed at its outer diameter). PT100 temperature sensors were located inside critical components and the temperature was measured for approximately 1 hour of operation. Figure 14 details the findings. As the temperatures appeared to be fine in atmospheric conditions, the system underwent further progress in terms of achieving higher and higher rotational velocities. This led to requiring testing with vacuum conditions. Similar approach was performed to uncover the temperature rises while operating with the vacuum conditions. The run was recorded with the nominal values from PT100s at the AMB coils and two different motor windings. The trial lasted approximately 1 hour and is shown in figure 15.

From the cooling lines, an estimation of the motor losses can be derived form the temperature difference of the cooling fluid. The rise in temperature was observed to

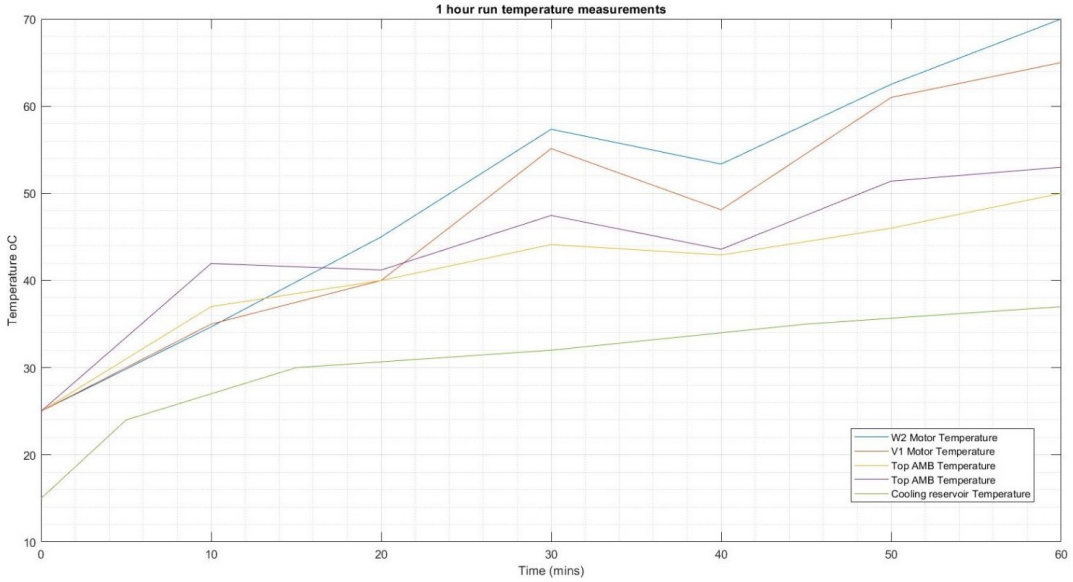

Figure 15: Prototype-2 motor winding and coolant temperature during 1 hour of continuous operation

be ΔT = 40°C. The flow was approximately 1 L/min (or 0.0167 kg/s), and the fluid was water.

Using the first law of thermodynamics, a simple calculation can be setup for the heat dissipated to the coolant:

$$\dot{Q} = \dot{m} C_p \Delta T \tag{32}$$

where $\dot{Q}$ is the heat transfer in kW, $\dot{m}$ is the mass flow rate, C_p is the specific heat capacity (for water C_p = 4182 J/kgK), ΔT is the change in temperature of the coolant.

Applying the numbers we gathered, we see the a total loss per phase of approximately 2.8 kW. If the total system is estimated to have a 94% overall efficiency as seen in the lower speed range of the efficiency curve, and the total output power is 100 kW then assuming the losses are all converted to heat, the heat generated by the motor system is of 120 kW*0.06 = 7.2 kW. As we have a 3 phase system, we can assume the losses are divided equally per phase, therefore 7.2kW/3 phases = 2.4kW of losses per phase. The estimated losses of 2.4 kW have an error of 14% from the actual losses of 2.8 kW. An explanation to the discrepancy can be from the simple reason that the motor has only been operated in the lower speeds, which require higher current and in turn heat the winding significantly more, exaggerating the losses.

5.2 Active magnetic bearings

5.2.1 AMB temperatures

The active magnetic bearings serve as a source of heat generation as the bias set of coils have a constant 7.5 A fed to it. The coils experience the same copper losses

explained in section 3.2.3 and therefore generate heat in the process. The actuators also experience iron losses similar to the motor, albeit the homopolar design mitigates the remagnetization hysteresys. These losses add to the heat generated in the overall system which can pass onto the rotor via radiation during vacuum operation.

At longer runs under vacuum conditions, it is crucial to know the subsystem's operational behaviours to prevent any surprises during commissioning of the machine. The AMB's were therefore tested under vacuum conditions of $5,6 * 10^{-3}$ mbar and full current (7.5 A) being fed to them. PT100 tempearture sensors were used to measure the temperature in the back of a few AMB coils. Figure 16 shows the temperature transient during 4 hours of operation.

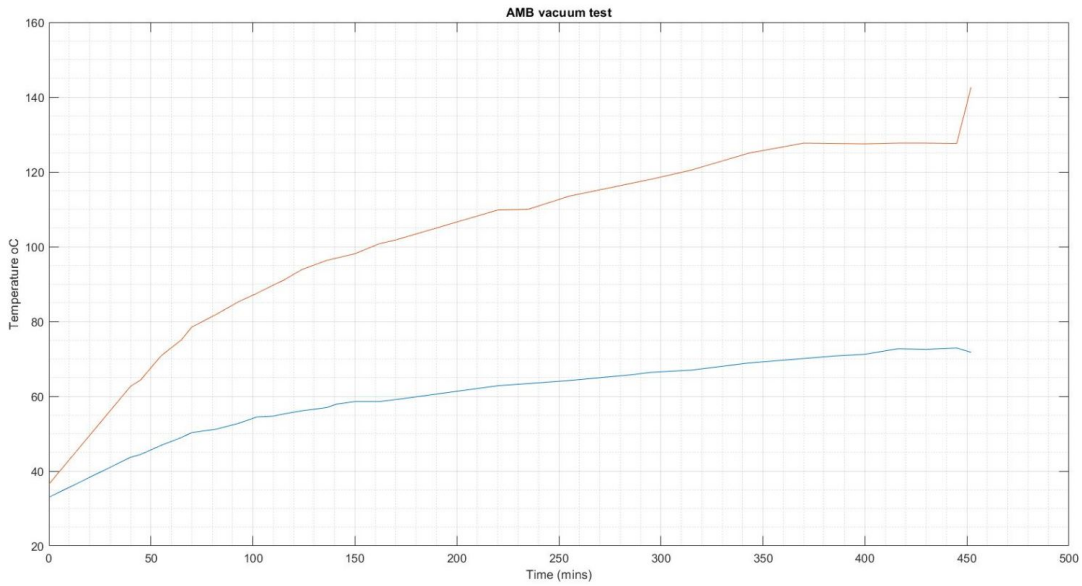

Figure 16: AMB temperature rise during vacuum operation

The plot shows the temperatures reaching steady state, which uncovered a potential future improvement to the machine. The highest temperatures for the AMB were where the PT100s were burried in the backs of the coils. The location has no direct view to another cooler surface and therefore serves a good location to check the maximum temperatures of 125-140°C. An interesting temperature behavior was the sharp temperature increase at the end of the run, where the vacuum pump was switched off and pressure slowly returned to atmospheric conditions.

Equation 32 can also be used to determine how much heat was produced by the coils during this 4 hour test. In total 37.24W heat was generated by the coils. This amount of heat is later cross-checked with simulated results.

6 Comparison

6.1 Motor

The comparison between the two methods proved beneficial in the loss discussion of the overall system. The results from the experimental runs and the ANSYS FEM simulations are overlaid and shown in figure 17. As seen in the graphs, the real

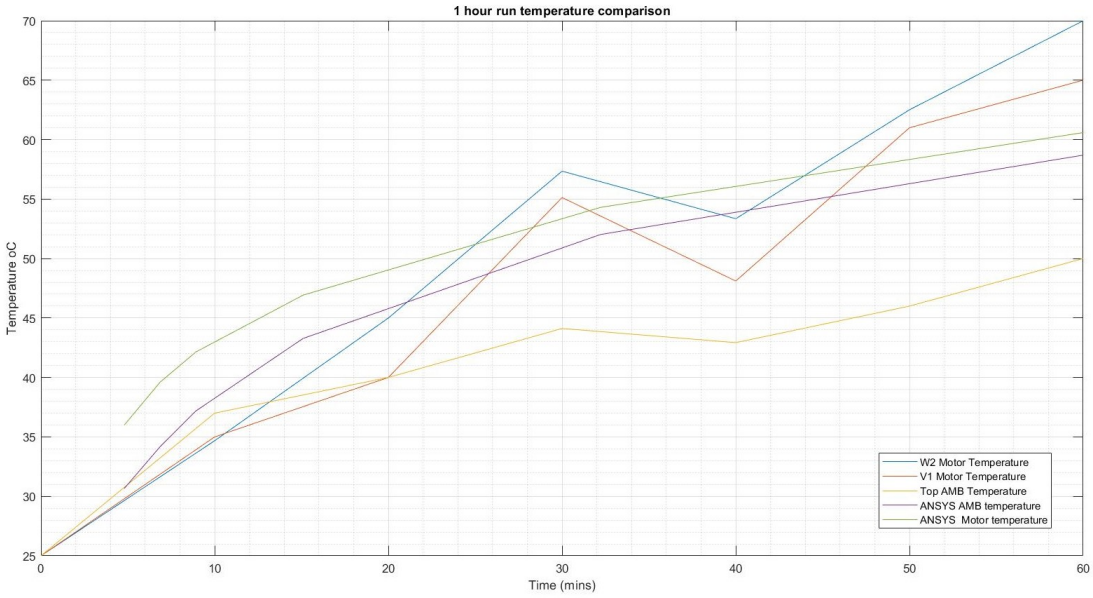

Figure 17: Motor temperature comparison between FEM simulation and experimental

temperatures acquired during the runs were higher than the simulated temperatures by 5-10°C. The graphs are, however, in line with one-another in regards to the temperature rise over the allotted time. This validates the simulation results as decent estimate of the system's thermal map. With some minor adjustments to the heating values of the simulation, it can be seen that the ANSYS model can predict with adequate accuracy where the temperature would settle after a few hours.

The current trials are no longer than a couple hours and with continual cooling of the windings, there have been no issues with a high temperature rise. The vacuum condition trials still require further investigation as the main focus up to this point was to increase the rotational speed before adding more complexity to the system.

As of the time of writing, the flywheel has been operated up to 7000 rpm, which does not allow the data to be collected in all ranges of operation. The speed limits at this point are a result of other subsystems that need improvement beyond the scope of this thesis. Based on these findings changes in the system can improve the motor sub-assembly and cooling unit to decrease the temperature rise seen. Paratherm LR [1] can be used as a coolant of choice with similar sized pumps in order to extract more heat from the motor windings. A two flow cooling system can also be implemented and a heat exchanger introduced to increase the effective heat dissipation. Additionally a cooling jacket could be designed to fit over the motor

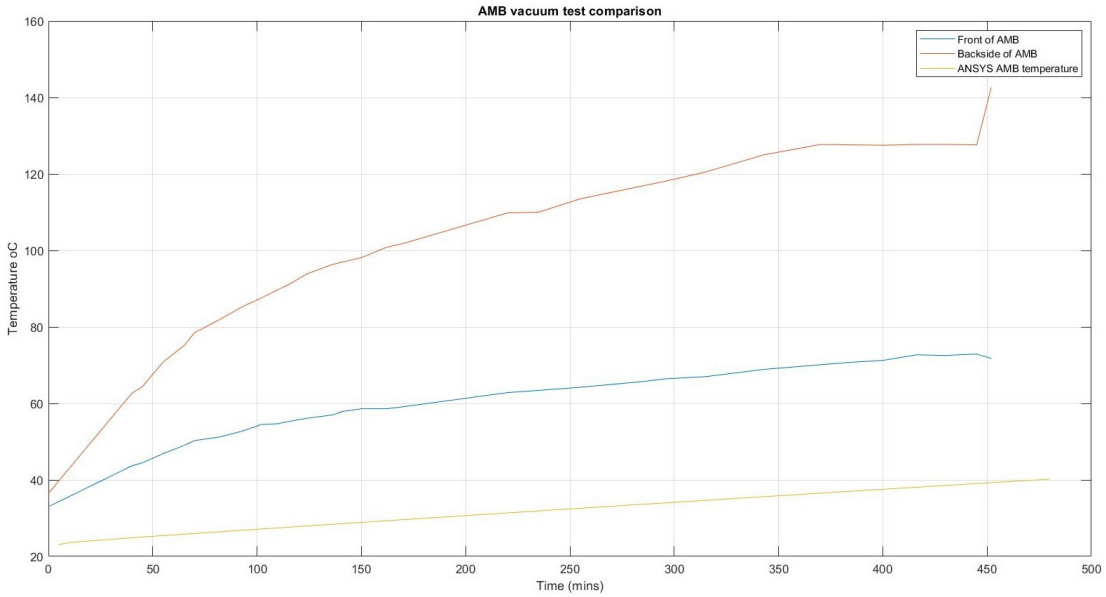

Figure 18: AMB temperature comparison between FEM simulation and experimental

coils. Within the next prototype iteration, the plan is to also add IR sensors to keep track of the rotor temperature itself as it is of primary interest. This could later be cross-checked with the results from ANSYS for further model validation.

6.2 Active Magnetic Bearing

In the experimental tests, the temperatures measured were typically higher than the initial simulated models. In comparison, the AMB vacuum temperatures were estimated to be around 40-50 °C when in reality they reached nearly 120 °C after 4 hours. Figure 18 demonstrates the discrepancy. This uncovered the fact that the AMBs were likely producing iron losses as well, which were not accounted for originally.

With the higher losses, a new design for the AMB stator was conceived (figure 19), where brass cooling lines could pass within the stator housing that holds the AMB actuators. This would effectively withdrawl an extra 250 W with a smaller pump and a convection coefficient of 0.2 $\frac{W}{mm^2K}$. This would ultimately allow the AMBs to settle at a temperature below 100 °C, however this detail still needs to be implemented in the actual system and verified experimentally.

In addition to the cooling lines, a redesign of the AMB actuators could be made where the actuator face is extended over the copper windings in order to decrease the flux drop between the poles of the actuators and therefore decrease the overall iron losses. A last method to improve the AMB system would be to add a permanent magnet embedded into the actuators in order to passively introduce a constant magnetic fields. In this method, the permanent magnet would replace the bias coils completely, decreasing the copper losses experienced by AMB windings. A redesign of the actuators is necessary to implement these changes and properly size the magnets

and chose the adequate magnetization grade.

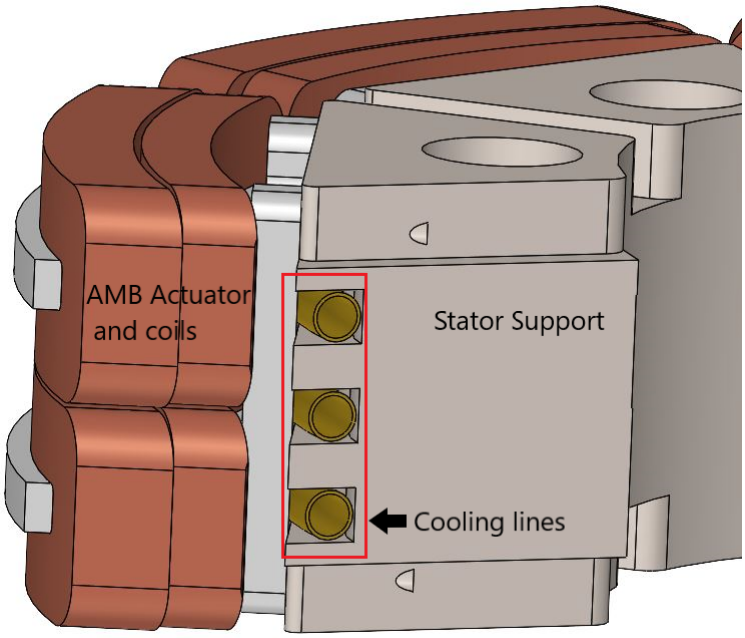

Figure 19: AMB stator side cooling design suggestion

6.3 Parameter Sensitivity

The simulation results are heavily dependant in the initial conditions and parameters used as input. The equation solver relies in the inputted parameters as a first step to iterate and every time step result is consequentially derived from the first iteration. The list below show the possible inputted parameters for the thermal analysis performed in ANSYS:

- Emissivity;
- Radiation emissive faces;
- Ambient temperature;
- Initial temperature;
- Internal heat generation;
- Film coefficient for convection exchange;

In order to accurately determine the effects of each variable, a standard model must be defined and act as the control. As a reminder, the nominal parameters of the simulation can be found in table 5 and will act as the control parameters.

Additionally, to simplify the study, only the properties that are able to be changed in the actual system will be analysed. From the aforementioned parameters, table 7 details the parameters further analysed and how they may be changed in the actual machine. The mentioned parameters can be directly controlled to a certain extent, therefore, the simulation could be changed to reflect the changes and check the sensitivity.

Parameter	Modification to machine and effect
Emissivity	Changing the surface finish of components
Initial temperature	Mimics temperature increase due to cycling
Heat generated	Different parts of the cycle would have different heat losses
Convective coefficient	Mimics changes in the cooling system

Table 7: Parameters chosen for sensitivity analysis

The output of most interest is the steady state temperature of different components and how that is affected with the changing parameters. For the reference simulation, the parameters used reflect the current configuration of the machine as seen in the previous chapters. For the sensitivity study, each of the parameters in table 7 was changed individually and the outputs were taken for the following cases:

Parameter	Change	Effect
Emissivity	decrease to 0.1	increased 1%
Emissivity	increased to 1	decreased by 5%
System initial temperature	increase to 52°C	increase of 20°C
Motor winding heat	increase of 10x	increase of 1.7%
Motor teeth heat	increase of 2x	increase of 40%
Convective coefficient	decrease to $3 * 10^{-5} \frac{W}{m^2 K}$	increase of 18%
Convective coefficient	increase to $3 * 10^{-1} \frac{W}{m^2 K}$	decrease of 2%

Table 8: Summary of parameter sensitivity study

The study revealed insights to each of the parameters. For the emissivity change between the rotor inner face and the outer stator face, the temperatures saw a difference of 5% at the rotor's maximum temperature. This change is taken into account and could help the system dissipate some of the excess heat. Although the surface-to-surface radiation between the outer housing surrounding the rotor is not simulated, the results suggest this could be a method of decreasing the rotor operational temperature. A matte black finish on the surface of the housing facing the rotor could have an emissivity of 0.97 and maximize the heat absorbed by the housing.

The study for the initial ambient temperature mimicked the cycling the machine would experience when charging and discharging frequently. As the initial temperature rose, the rotor temperature was the most affected. With a 20°C increase in temperature, the rotor also experienced a 20°C increase overall. This is of special significance when piloting the machine for frequent cycling and requires a further study to mitigate this temperature build up.

The internal heat generated demonstrated how sensitive the machine is to increases in the losses of the motor and AMB. At first, the copper losses were increased. The motor copper losses demonstrated little effect on the temperature of the rotor. Likely due to the direct cooling located at the windings. The copper losses were increased by ten with little effect on the rotor temperature itself (less than 2%). The increase in iron losses, however, gave drastically different results. By doubling the heat generated by the motor teeth, the system experienced an 40% increase in temperature. An actual increase in the iron losses is not likely as these are dependent on the rotation of the fields, therefore limited by the rotor's top speed. This result, however, is relevant for any new comparable machine that would require higher operational speeds.

Lastly, for the convection coefficient, a 18% temperature increase was observed as the convection coefficient decreased, simulating a decrease in effective heat withdrawn by the cooling system. The temperature increase was expected, however, the inverse was not true. The cooling coefficient would aid in the temperature closest to the motor coils logarithmic, meaning, as the convection coefficient increased, the amount of power dissipated would not scale linearly. This suggests that improvements to the cooling alone would see diminishing returns and therefore should not be the only focus.

Overall the parameter analysis performed establishes the limits of the simulation software, but furthermore it demonstrates which improvements will aid the temperature control the most.

7 Summary

This paper presents methods for thermal analysis for a flywheel storage system under vacuum conditions. The calculated values from the theory section were utilized in order to design an actual system and simulations were performed to estimate the temperature curves seen by the built machine. Isolated models of the subsystems were carefully analyzed in the simulation section and then later compiled into a larger overall system model which gave results in-line with the measured temperatures of the machine.

From the simulation initial results were gathered in order to foresee the temperature rises of the machine. Once actual results were gathered, seen in section 5.1.1, and compared to the simulated results, it was observed that the machine produced more losses than in the simulations. From there the simulation parameters and boundary conditions were changed to better reflect the system behavior.

The simulations gave a good sense of the expected temperatures and how the rotor of the flywheel and its individual components would be affected by the heat generated from the motor and active magnetic bearing assemblies.

Although the system's thermal control is successful in containing vulnerable components under critical temperature, there are key areas of improvement for the next iteration as detailed in chapter 6. These are listed in the list below in order of importance and feasibility

- Inclusion of IR sensor to monitor rotor temperature;
- Coolant change from deionized water to Paratherm LR;
- Electrically insulate the motor temperature sensors to avoid interference;
- Rotor motor yoke back iron implementation;
- Design change of AMB actuator to include cooling lines;
- Design change to AMB actuators to decrease iron losses;
- Motor stator design change to decrease iron losses;
- Implementation of rotor cooling jacket design;
- Redesign AMB actuators to replace the bias coils with a permanent magnet;
- Consider other motor topology for lower idling losses.

As the Prototype-2 improves and surpasses its current speed limit, the information learned through the simulations and the measured experiments will serve as a foundation in which to move forward with not only the successful commissioning of Prototype-2 into a piloting phase, but for future endeavors of the company as well.

References

[1] Paratherm LR ® datasheet. 2003.

[2] F. D. D. Bergman, T.; Lavine, A.; Incropera. *Fundamentals of Heat and Mass Transfer*. 2011.

[3] J. Budynas, Richard G; Nisbett. *Shigley's Mechanical Engineering Design*, volume 4. 2016.

[4] Y. A. Cengel. Heat Transference a Practical Approach. *MacGraw-Hill,*, 4(9):874, 2004.

[5] H. W. Cho, H. K. Sung, J. Y. Choi, D. J. You, J. H. Park, S. M. Jang, and S. H. Lee. Analytical calculation of rotor losses in high-speed permanent magnet synchronous motor at different load conditions. *Journal of Applied Physics*, 103(7):1–5, 2008.

[6] Cogent. Typical data for SURA ® M270-35A Cogent. Technical Report June, 2008.

[7] M. Grönlund. *Stator core material selection for kinetic energy storage*. PhD thesis, Tampere Univeristy of Technology, 2018.

[8] J. Huang, S. S. Naini, R. Miller, D. Rizzo, K. Sebeck, S. Shurin, J. Wagner, and S. Member. A Hybrid Electric Vehicle Motor Cooling System—Design, Model, and Control. 68(5):4467–4478, 2019.

[9] IEA. World Energy Balance 2020, 2020.

[10] A. Jäger-Waldau. *Jrc Science for Policy Report*. 2019.

[11] Luvata. Copper hollow conductors. Technical report, 2018.

[12] A. Mahmoudi, W. L. Soong, G. Pellegrino, and E. Armando. Efficiency maps of electrical machines. *2015 IEEE Energy Conversion Congress and Exposition, ECCE 2015*, (2015):2791–2799, 2015.

[13] T. S. Nielsen. *Handbook of Small Electric Motors, Ch.10*, volume 7900. 2014.

[14] E. Nitsche and M. Naderer. Internally Cooled Hollow Wires Doubling the Power Density of Electric Motors. *ATZelektronik worldwide*, 12(3):42–47, 2017.

[15] H. Rashid. *Power Electronics Handbook*. 2017.

[16] H. Schaede, M. Richter, L. Quurck, and S. Rinderknecht. Losses in an Outer-Rotor-Type Kinetic Energy Storage System in Active Magnetic Bearings. pages 342–346, 2014.

[17] S. Sharkh, J. Renedo-anglada, and M. Yuratich. Rotor losses in PM synchronous machine. 2019.

[18] M. Strasik. Design , Fabrication , and Test of a 5 kWh Flywheel Energy Storage System Utilizing a High Temperature Superconducting Magnetic Bearing. *Technology*, pages 1–12, 2010.

[19] Www.Emetor.com/windings/. Emetor motor winding calculator.